

Provided for non-commercial research and education use.
Not for reproduction, distribution or commercial use.



This article appeared in a journal published by Elsevier. The attached copy is furnished to the author for internal non-commercial research and education use, including for instruction at the authors institution and sharing with colleagues.

Other uses, including reproduction and distribution, or selling or licensing copies, or posting to personal, institutional or third party websites are prohibited.

In most cases authors are permitted to post their version of the article (e.g. in Word or Tex form) to their personal website or institutional repository. Authors requiring further information regarding Elsevier's archiving and manuscript policies are encouraged to visit:

<http://www.elsevier.com/copyright>



Contents lists available at ScienceDirect

Cold Regions Science and Technology

journal homepage: www.elsevier.com/locate/coldregions

Sea ice thickness measurements by ultrawideband penetrating radar: First results

Benjamin Holt ^{a,*}, Pannirselvam Kanagaratnam ^b, Siva Prasad Gogineni ^c, Vijaya Chandran Ramasami ^c, Andy Mahoney ^d, Victoria Lytle ^c^a Jet Propulsion Laboratory, California Institute of Technology, 4800 Oak Grove Drive, Pasadena, CA, 91109, USA^b Benaforce Sdn. Bhd., Shah Alam 4000, Malaysia^c CReSIS, University of Kansas, 2335 Irving Hill Road, Lawrence, KS, 66045, USA^d National Snow and Ice Data Center, Boulder CO 80303, USA

ARTICLE INFO

Article history:

Received 10 September 2007

Accepted 16 April 2008

Keywords:

Sea ice

Sea ice thickness

Penetrating radar

Electromagnetic modeling

ABSTRACT

This study evaluates the potential of ultrawideband penetrating radar for the measurement of sea ice thickness. Electromagnetic modeling and system simulations were first performed to determine the appropriate radar frequencies needed to simultaneously detect both the top ice surface (snow–ice interface) and to penetrate through the lossy sea ice medium to identify the bottom ice surface (ice–ocean interface). Based on the simulation results, an ultrawideband radar system was built that operated in two modes to capture a broad range of sea ice thickness. The system includes a low-frequency mode that operates from 50–250 MHz for measuring sea ice thickness in the range of 1 to 7 m (both first-year and multiyear ice types) and a high-frequency mode that operates from 300–1300 MHz to capture a thinner range of thickness between 0.3 and 1 m (primarily first-year ice type). Two field tests of the radar were conducted in 2003, the first off Barrow, Alaska, in May and the second off East Antarctica in October. Overall the radar measurements showed a mean difference of 14 cm and standard deviation of 30 cm compared with in situ measurements over first-year ice that ranged from 0.5 to 4 m in thickness. Based on these initial results, we conclude that ultrawideband penetrating radar is feasible for first-year sea ice thickness measurements. We discuss approaches for further system improvements and implementation of such a system on an airborne platform capable of providing regional sea ice thickness measurements for both first-year and multiyear ice from 0.3 to 10 m thick.

© 2008 Elsevier B.V. All rights reserved.

1. Introduction

The thickness of sea ice is the integrated result of heating and forcing from the atmosphere and ocean and has long been considered a key indicator of climate change in the polar regions. The Arctic is undergoing significant changes in sea ice properties, including thickness and extent, that are indicative of a rapidly changing environment at the least, likely induced by warming from increasing greenhouse gases (e.g. ACIA, 2005; Richter-Menge et al., 2006; IPCC, 2007). A significant reduction in the mean thickness of the perennial Arctic sea ice occurred during the 1990s as compared with earlier decades (Rothrock et al., 1999, 2003), based on submarine-mounted upward looking sonar (ULS) measurements of ice draft. Since 1979, sea ice extent has undergone dramatic declines in both the summer minima (Stroeve et al., 2007) and winter maxima (Meier et al., 2005). The perennial ice component of the Arctic is rapidly diminishing in extent and age (Kwok, 2007). In the Antarctic, it is unknown if thickness is changing due to a lack of observations, however, the

extent of the ice cover appears to be slightly increasing (Liu et al., 2004).

What remains largely unknown is how the mass balance or volume of sea ice is changing both in terms of the fractional area and distribution of sea ice thickness. Yu et al. (2004) used submarine ULS data to determine that, over recent decades including the 1990s, the fraction of open water and first-year ice increased while that of thicker ice decreased. Most of these changes were attributed to increased ice export of the perennial ice out of Fram Strait, but some to variability in thermal forcing. Rothrock and Zhang (2005) suggest that the bulk of the volume loss is due to reduced growth in undeformed ice. In contrast, a 12-year time series of seasonal ice properties using moored ULS data found little statistical change in first-year undeformed ice within the Canadian Beaufort Sea (Melling et al., 2005). Lindsay and Zhang (2005) suggest that there is both a reduction in ridges and thinning in undeformed ice taking place. Synoptic-scale measurements of sea ice thickness at regular intervals are required to improve the understanding of sea ice mass balance and hence how sea ice is changing within the global heat balance and ocean thermohaline circulation.

Despite its fundamental importance, sea ice thickness is one of the most difficult measurements to obtain on synoptic and climatic scales,

* Corresponding author. Tel.: +1 818 354 5473.

E-mail address: Ben.Holt@jpl.nasa.gov (B. Holt).

including from satellites (U.S. National Research Council, 2001). A wide range of sea ice thickness measurement approaches exist (Fig. 1) (Wadhams, 2000; Haas, 2003), starting with the accurate point-source measurements made by augers and thermistor chains, to inferred thickness measurements obtained by upward-looking (e.g. Rothrock et al., 1999) and side-scan sonar (Wadhams et al., 2006) that measures ice draft, to measurements of sea ice height (freeboard) by both laser and radar altimeters from aircraft and satellites (Laxon et al., 2003; Forsberg and Skourup, 2005; Kwok et al., 2007). The satellite laser altimeter measurements of freeboard have been used to make initial estimates of sea ice thickness, based on assumptions of snow and ice density, snow depth, and a statistical relation of freeboard to overall thickness (Zwally et al., in press). Another capability makes use of electromagnetic induction (EM) sensors mounted on surface sleds or low-flying helicopters that produce high-density thickness transect measurements up to many kilometers in length and are currently often utilized during sea ice field experiments (e.g. Kovacs and Holladay, 1990; Multala et al., 1996; Haas, 1998, 2003; Worby et al., 1999). The EM measurements are made using frequencies between 1 and 200 kHz to detect the ice bottom surface. Final EM thickness derivations require estimation of the top ice surface that is usually determined with in-situ snow depth measurements and ice surface height obtained from a companion laser.

While all of these approaches are valuable, thickness measurements remain sparse and the accuracies and capabilities of the range of approaches vary. A remote sensing method that detects both the top and bottom ice surfaces over a wide range of thicknesses that could be implemented on an airborne (including robotic) or satellite platform would be of great scientific value. Obtaining thickness measurements over a wide region at weekly or monthly temporal sampling rates would significantly improve the understanding of the changes in the thickness distribution and sea ice mass balance that are currently taking place particularly in the Arctic regime and potentially in Antarctica as well.

In this study we examine the potential of penetrating radar to measure sea ice thickness by the simultaneous detection of the top and bottom ice surfaces. The use of penetrating or sounding radar for measuring sea ice thickness has been previously examined with limited success. These efforts show that penetration depth increases with lower frequencies but range resolution at these lower frequencies was limited largely by technology. Direct penetration of thicker sea ice was found to require the use of frequencies in the range of P-band (400 MHz) and lower to overcome the high attenuation from the lossy sea ice medium and detect the ice–ocean interface (Kovacs and Morey, 1986; Winebrenner et al., 1995). Several studies used surface-

based step-frequency and impulse ground penetrating radars to sound sea ice (Kovacs and Morey, 1979, 1986; Izuka et al., 1984; Okamoto et al., 1986; Sun et al., 2003). These systems are limited, particularly as flown on airborne platforms, by the low effective pulse repetition frequency (PRF). More specifically, the time required to obtain a measurement does not support the PRF needed to sample the Doppler frequency induced by the aircraft motion. For a radar operating at 1000 MHz with an antenna beamwidth of 60° and aircraft speed of 50 m/s, the maximum Doppler frequency is about 166 Hz. This requires a minimum PRF of about 500 Hz with a guard band. The effective PRF of typical impulse radars is not lower than the 500 Hz needed to adequately sample the Doppler frequency. These previous studies found difficulties in the actual detection of the ice–ocean interface, including within the thicker ice regimes, due to the presence of voids, scattering from adjacent ridges/keels, and the varying dielectric response within the bottom ice or dendritic layer. As with EM measurements, difficulties were also found with highly varying ice thickness. Now, recent advances in RF, microwave, and digital device technologies offer the unique capability of implementing high-sensitivity, wideband coherent radars that overcome many of the previous technology difficulties and make a penetrating radar for sea ice thickness feasible.

Our measurement design goals are to measure sea ice thickness across a range of 0.3–10 m with accuracy on the order of 25 cm (e.g. Thorndike et al., 1992), which is better than current remote sensing capabilities and approaches the climate objective of 10 cm (Integrated Global Observing Strategy, 2007). With a long-term goal of understanding the sea ice mass balance, a key is to capture the broadest thickness range possible to assemble representative ice thickness distributions, the primary statistical parameter used for the comprehensive understanding of thickness changes (Thorndike et al., 1975; Wadhams, 2000). This leads to the need to measure thickness to determine the major forms of sea ice present, seasonal growth rates, and regional and annual differences (Thorndike et al., 1992). The 25-cm measurement goal is approximately equivalent to a precision requirement of 2–4 cm for altimetry methods to derive freeboard. The measurement range accounts for the primary thickness distribution components of sea ice mass, particularly for the thicker deformed ice which are presently under-sampled by all other techniques and account for the largest unknown contribution to the overall sea ice mass balance. In terms of a satellite or airborne implementation, a single-pass system is also desirable as the ice cover moves nearly continuously over short time scales (Kwok et al., 2003). This rapid motion sharply reduces the high surface correlation required for the use of one possible measurement approach, that is repeat-pass radar interferometry (Rosen et al., 2000). The horizontal sampling requirements are less straightforward to determine, as there is a general lack of suitable measurements that assesses thickness variability particularly for the thicker ranges. The radar will produce an integrated return for each detected measurement, so the sampling should be small enough so that the presence of deformed ice and its impact on the overall mean thickness can be identified. The horizontal resolution for a single thickness value from an airborne platform should be at least 50 m and preferably in the range of 10–20 m or less.

The radar system design also incorporates the use of very wide bandwidth to obtain both the desired vertical resolution over a range of thicknesses as well as to identify the snow–ice interface, requiring higher frequencies than those needed to detect the ice–ocean surface. As described by Elachi (1987), the bandwidth B is related to the pulse length τ where $B = 1/\tau$, so the vertical resolution r can be determined as follows:

$$\Delta r = C \tau / 2 = C / 2B, \quad (1)$$

with C equal to the speed of light. Thus increasing bandwidth improves vertical resolution. A similar ultrawideband approach was recently applied to the measurement of snow thickness over sea ice,

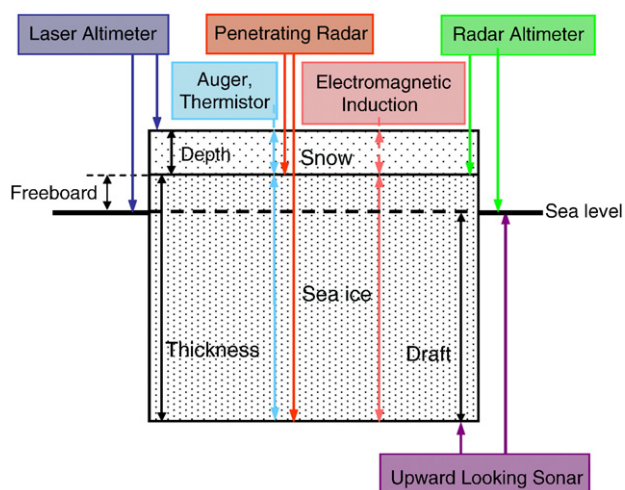


Fig. 1. Schematic of various ice draft/freeboard/thickness measurements.

using a higher frequency range of 2–8 GHz (Kanagaratnam et al., 2007). This radar system detects the top of the snow as well as the snow–ice interface, with a frequency range designed to provide finer vertical resolution (2–3 cm) of the generally thinner and more radar-transparent snow layer as compared to the underlying sea ice cover.

To provide guidance for the system design, we developed a series of radar simulations to identify the optimal radar frequencies for varying sea ice thicknesses and properties (Section 2). We first constructed geophysical models of primary sea ice types to characterize their physical composition and structure. Next, simple electromagnetic models were developed that used the permittivity profiles generated from the geophysical models and then simulations were run based on the electromagnetic models. From the simulation results, we designed and implemented a prototype radar operating in a frequency-modulated continuous wave (FM-CW) mode (Section 3). The radar system extends down to frequencies as low as 50 MHz, which are needed for penetration to the ice–ocean bottom of the thicker components of the sea ice thickness distribution including deformed ice. Higher frequencies are needed to detect the snow–ice interface, where sufficient penetration is needed to extend through the snow layer but not beyond the snow–ice interface. With sufficient penetration, the system makes use of the high dielectric contrast at the ice–ocean interface to obtain a strong return that is dependent on bottom roughness properties and slope. The final prototype radar has two modes: a low-frequency mode that operates from 50 to 250 MHz (which falls within the very high frequency (VHF) range) to measure the thicker ice components greater than about 1 m, and a high-frequency mode using a frequency range from 300 to 1300 MHz (ultra high frequency or UHF) to capture ice thinner than 1 m. The specific range of frequencies of both modes enables penetration of the thicker ice while retaining sensitivity to thinner ice and the top ice surface. As described in Section 4, the initial tests of the radar were conducted in the Arctic in May 2003 and in the Antarctic in October 2003. Both field tests were done in conjunction with in situ sea ice and snow thickness measurements for validation. Section 5 provides a summary and discussion on future system improvements needed to move the instrument towards an airborne implementation.

2. Sea ice radar scattering modeling and simulations

In this section we briefly describe the sea ice characteristics that affect radar scattering and the development of simple scattering electromagnetic models followed by the results of simulations that were used to guide the system design. We represent sea ice as a multi-layered medium, where each layer is characterized by its dielectric constant, density, and average particle size. The nadir penetrating radar must detect both the top and bottom of the sea ice layer over a wide range of thicknesses and with a satisfactory vertical resolution.

2.1. Sea ice characteristics and radar scattering model

A broad range of surface and internal characteristics of sea ice determine the radar scattering from sea ice and its overlying snow cover (e.g. Tucker et al., 1992). These properties include salinity and temperature, surface roughness, crystal structure, brine inclusions and air pockets, thickness, and electromagnetic properties. The properties vary by ice age and season. Deformation occurs at many scales under a wide range of conditions and imparts considerable change to the top and bottom ice surface roughness as well as internal properties related to block size and voids. Sea ice is a complex and lossy medium, so a radar scattering model must account for the heterogeneous nature of sea ice, surface and volume scattering, dielectric properties, penetration depth, radar frequencies and radar incident angle (Hallikainen and Winebrenner, 1992).

To characterize both winter first-year and multiyear ice, we used detailed profiles of physical observations from Arctic winter modeled

first-year (Cox and Weeks, 1988; Kovacs et al., 1987a) and a multiyear ice core (Kovacs and Morey, 1986), where the salinity, temperature, and bulk density were known at 5 and 10 cm intervals, respectively, from which brine and air volume and ice density were calculated. We computed the complex permittivity of each depth from these data using a dielectric mixture model. Then we used the density and average size of brine inclusions and air pockets to compute an effective dielectric constant that accounts for volume scattering effects. The interface between the bottom sea ice layer and seawater was modeled as a dendritic interface. Various simulations were performed using different ranges of radar frequencies.

2.1.1. Sea ice dielectric constant

A dielectric mixture model developed by Tinga et al. (1973) was used to compute the dielectric constant of sea ice from published salinity, temperature, and brine and air volume fraction data. The sea ice dielectric constant is expressed as a function of the dielectric constants of the constituents (pure ice and brine) and their volume fractions. The mixture dielectric constant is given by the following formula,

$$\frac{\epsilon_M - \epsilon_1}{\epsilon_1} = \frac{V_1}{V_2} \frac{\epsilon_2 - \epsilon_1}{\left(-\left(\frac{V_2}{V_1}\right)n_1(\epsilon_2 - \epsilon_1) + n_2(\epsilon_2 - \epsilon_1) + \epsilon_1\right)} \quad (2)$$

where (ϵ_1, ϵ_2) , (V_1, V_2) , (n_1, n_2) are the dielectric constants, volume fractions, and depolarization coefficients of the host-medium (pure ice) and the inclusions (brine), respectively, and ϵ_M represents the dielectric constant of the heterogeneous mixture. The depolarization coefficient accounts for the shape and orientation of the brine inclusions with respect to the electric field. The values of the dielectric constant of pure ice and brine were computed using the well-known formulae developed by Debye (1929). We used empirical relations presented in Cox and Weeks (1983) to determine the volume fractions of brine in sea ice from the salinity, density and temperature ice profile data. Using the above model, the sea ice dielectric loss factor, which affects attenuation and penetration depth, was computed for ice salinities of 2 and 3 psu (characteristic of multiyear ice) and an ice temperature of -10°C and then plotted as a function of frequency assuming random orientation (Fig. 2). The loss factor of sea ice is low in the frequency ranges from 1 to 100 MHz (10^6 – 10^8 Hz), with the basic curve from 100 MHz to 10 GHz (10^8 – 10^{10} Hz) matching reasonably well with previous results (Vant et al., 1978; Kovacs et al., 1987b). The decrease in the loss factor between 10 MHz and 500 MHz is due to frequency-dependent electromagnetic brine

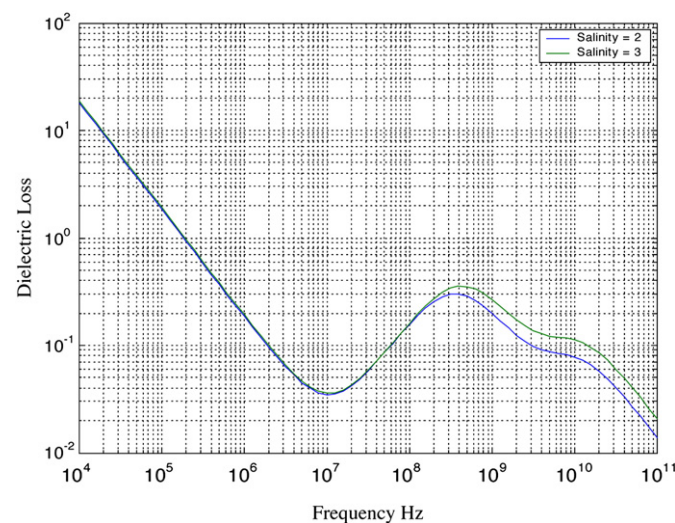


Fig. 2. Modeled dielectric loss factor of sea ice for salinities of 2 and 3 psu at -10°C .

properties. The relaxation process of brine is in effect for frequencies higher than 1 GHz. The real part of the dielectric constant of sea ice is approximately in the range of 3–4 for this same approximate range of frequencies (100 MHz to 10 GHz) and shows a gradual decrease with increasing frequency (Vant et al., 1978; Kovacs et al., 1987b).

2.1.2. Volume scattering

We account for the volume scattering effects due to brine inclusions and air pockets by using effective medium approximation to compute the attenuation loss caused by volume scattering. Under this approximation, effective permittivity, ϵ_{eff} , is given by (Kong, 1986):

$$\epsilon_{\text{eff}} = \frac{1 + 2f_v(\epsilon_s - \epsilon_b)/(\epsilon_s + 2\epsilon_b) - j2f_vk^3a^3 | \frac{(\epsilon_s - \epsilon_b)/(\epsilon_s + 2\epsilon_b)}{1 - f_v(\epsilon_s - \epsilon_b)/(\epsilon_s + 2\epsilon_b)} |^2 (1 - f_v)^4}{1 - f_v(\epsilon_s - \epsilon_b)/(\epsilon_s + 2\epsilon_b)} \quad (3)$$

where f_v represents the fractional volume occupied by the inclusions, ϵ_s represents the permittivity of inclusions, ϵ_b is the permittivity of the background material, a is the radius of inclusions, and k represents the wavenumber. Volume scattering is more important at the higher end of the frequency ranges under consideration.

2.1.3. Ice–ocean interface

The real part of the dielectric constant of seawater is about 80. In the ideal case with a planar interface, the high dielectric contrast between sea ice (real part=3–4) and ocean will result in a large reflection of the radar energy from the ice–ocean interface. However, most sea ice has a groove-shaped vertically oriented dendritic layer at the ocean interface, which is also referred to as the skeletal layer, ice lamellae or platelets (Weeks and Ackley, 1986). The dendritic layer ranges from 1–5 cm in thickness (height) and length with spacing of the platelets between 0.8 to 1 mm (Weeks and Ackley, 1986; Tucker et al., 1992). The horizontal orientation of the dendrites coincides with the direction of the underlying ocean current. The dendritic layer is porous with complicated profiles of salinity and temperature that result from ice formation, salt rejection, and heat flux occurring within this thin layer.

In terms of radar reflectivity, the dendritic layer presents a smooth impedance transformation from the low sea–ice dielectric constant at the top of the dendrite layer to the high seawater dielectric constant at the bottom of the dendrite layer. Kovacs and Morey (1979, 1986) found the thickness and orientation, in these cases anisotropic, of the

dendritic axis to be important relative to the impulse radar wave orientation and radar return strength, and thus the overall detectability of ice thickness. This impedance match is very prominent at the higher microwave frequencies where the radar wavelength is comparable to the length and thickness of the transitional layer.

Because of the wide radar beamwidth and use of generally lower frequencies, we assumed the dendritic layer to have random orientation. We modeled this impedance matching effect using an exponential variation for the dielectric constant along this interface, as given below:

$$\epsilon(x) = \epsilon_1^{(1-\frac{x}{d})} \epsilon_2^{\frac{x}{d}} \quad (4)$$

where (ϵ_1, ϵ_2) are the dielectric constants of sea ice and seawater respectively, x is the thickness and d is the length of the dendritic interface.

The ice–ocean interface also includes various scales of surface roughness, produced by turbulence, melting processes, and deformation. If this roughness has similar scales to the radar wavelengths that penetrate to the ice–ocean interface, there will be additional scattering (Bragg scattering) that will reduce the intensity of the reflected signal from the ice–ocean interface. Little is known quantitatively about the ice–ocean surface roughness at the radar wavelength scales between a few centimeters up to 2 m (100 MHz) or so. Goff et al. (1995) provide quantitative estimates of bottom roughness at longer scales. The top surface roughness will be more important at the higher frequencies that are under consideration. Manninen (1997) derived quantitative estimates of surface roughness at many scales. We did not include top or bottom ice surface roughness, beyond the scale of the dendritic layer, in the simulations. Also, we did not include a snow layer, whose impact at the considered frequencies and with a nadir-viewing radar are thought to be comparatively minor (Kanagaratnam et al., 2007).

2.2. Radar model simulations results

Using the model described in the previous section, we performed simulations based on published sea ice core properties. For first-year ice, we used modeled ice temperature and salinity data of Cox and Weeks (1988) with additional calculations of bulk sea ice density, brine volume, and ice density based on the calculations of Cox and Weeks (1983). The first-year sea ice data used were for 0.76 m and 1.22 m thick ice (summarized in Kovacs et al., 1987a), with values of

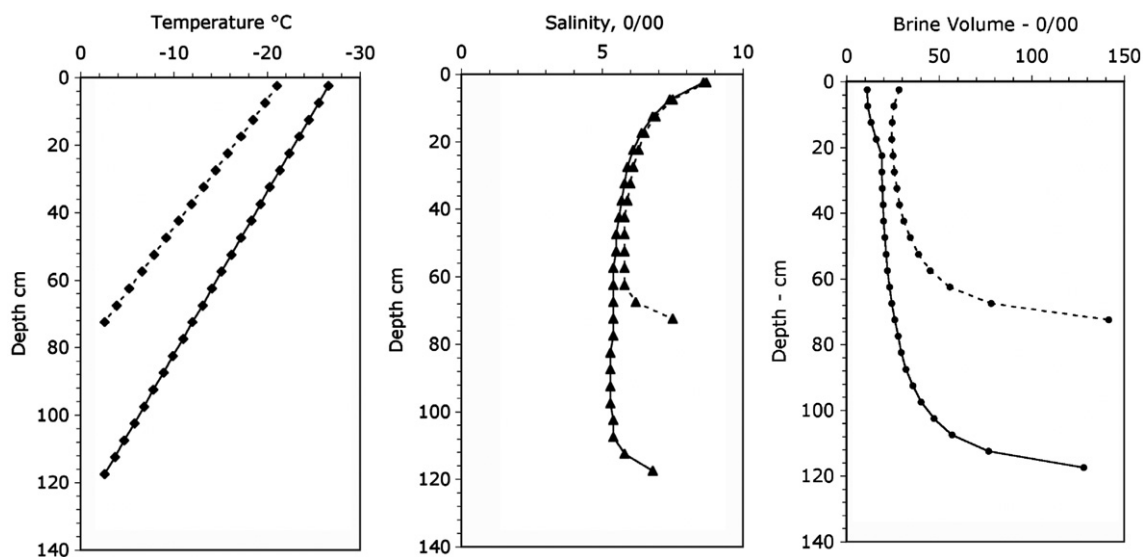


Fig. 3. Modeled first-year sea ice properties used in simulations for 0.76 m and 1.22 m cores from Cox and Weeks (1988) and Kovacs et al. (1987a). See text for more details.

Table 1
Sea ice thickness ultrawideband radar system parameters

System parameters	MODE 1 (VHF – thick ice)	MODE 2 (UHF – thin ice)
Chirp frequency range	50–250 MHz	300–1300 MHz
Unambiguous range	3–30 m	0.5–5 m
Transmit power	20 dBm	20 dBm
Chirp time	2 ms	10 ms
Range resolution	75 cm	15 cm
Sampling frequency	500 kHz	500 kHz
Antenna feed-thru (1 m long cable)	950 Hz	950 Hz
Maximum unambiguous range	30 kHz	6 kHz

temperature, salinity, and brine volume plotted in Fig. 3 for both thicknesses. For perennial ice, we used ice core data obtained from a 7.35 m multiyear ridge off the Alaskan Beaufort Sea coast, one of the thickest multiyear cores we were able to identify in the open literature that included thin (10 cm) samples (Kovacs and Morey, 1986, their Table 1). The measured multiyear ice values of salinity and temperature and the calculated values of brine volume (likewise derived following the procedures of Cox and Weeks, 1983) are shown in Fig. 4. The top 2 m of the core are above sea level while the presence of a slushy zone was noted near the keel bottom.

We present results of model simulations that justify the choice of the final radar operating frequencies, which include the following linear FM Chirp configurations: a) 1–2 GHz (L-band); b) 300–1300 MHz (UHF); and c) 50–250 MHz (VHF) systems. We assumed that the radar is mounted 1 m above the ice in all cases shown. Based on Eq. (1), the first two configurations have theoretical vertical resolutions of 15 cm, while the VHF configuration has a resolution of 75 cm (Table 1).

2.2.1. First year ice

Fig. 5 shows the return power vs. range obtained using the L-band (1–2 GHz) FM radar using modeled dielectric properties of 0.76 m thick first year ice and a 3-cm thick dendritic layer. The reflected power from a planar bottom (ice–water) interface is about 20 dB below that from the top surface reflection (snow–ice interface is located at about 70 cm) and is clearly identifiable in the range profile

(at about 150 cm). The inclusion of the dendritic layer reduces the reflected power at the ice–water interface by about another 13 dB, which is due to the impedance match of this layer between sea ice and seawater. The reflection using the dendritic interface is about 32 dB below the snow–ice interface reflection, and hence it is almost lost within the range sidelobes of the top interface. When a Hamming window, a signal processing linear filter designed to suppress the sidelobes (weaker portions of the radiation beam pattern which are not the main beam), is applied at the received signal, it is possible to see the ice–water reflection, which becomes about 8 dB above the reduced range sidelobes. The sharpness of the peaks from the top and bottom ice returns indicates there is sufficient resolution with the 1000 MHz bandwidth at least for this ice thickness. However, the level of signal above the sidelobes or signal-to-noise ratio (SNR) is likely insufficient for identifying the bottom interface over a wide range of operating conditions. A radar is needed with more than 50–60 dB sidelobes which is realizable using today's technology (Misaridis and Jensen, 2005). In addition to the impedance matching effects, the dielectric losses at L-band frequencies also result in significant reduction in the reflected power.

The same experiment was repeated with the UHF (300–1300 MHz) FM radar system configuration (Fig. 6). The reflected power from the planar bottom interface is detected about 15 dB below the surface reflection and has higher overall return than in the 1–2 GHz simulation (Fig. 5). The effect of the dendrite interface on the range profile is reduced (about 6 dB) compared to that on the 1–2 GHz range profile (about 13 dB), as the dendritic layer appears almost planar at the lower frequencies. Use of the Hamming window results in the bottom interface being about 20 dB more than the range sidelobes of the top ice surface reflection. This SNR is sufficient for identifying the ice–ocean interface and hence we can get an accurate estimate of the sea ice thickness. As above, we can see that the 300–1300 MHz radar has sharp peaks, indicating good range resolution for 0.76 m and for 1.22 m ice as well (latter not shown).

Lastly, the range profile for the VHF (50–250 MHz) system is shown in Fig. 7. As expected, there is no impact from the presence of the dendritic layer at these lower frequencies compared to the higher frequency simulations. However, the broad multiple peaks indicate the lack of sufficient range resolution to isolate the snow–ice and ice–water returns for this first-year ice, due to the relatively low

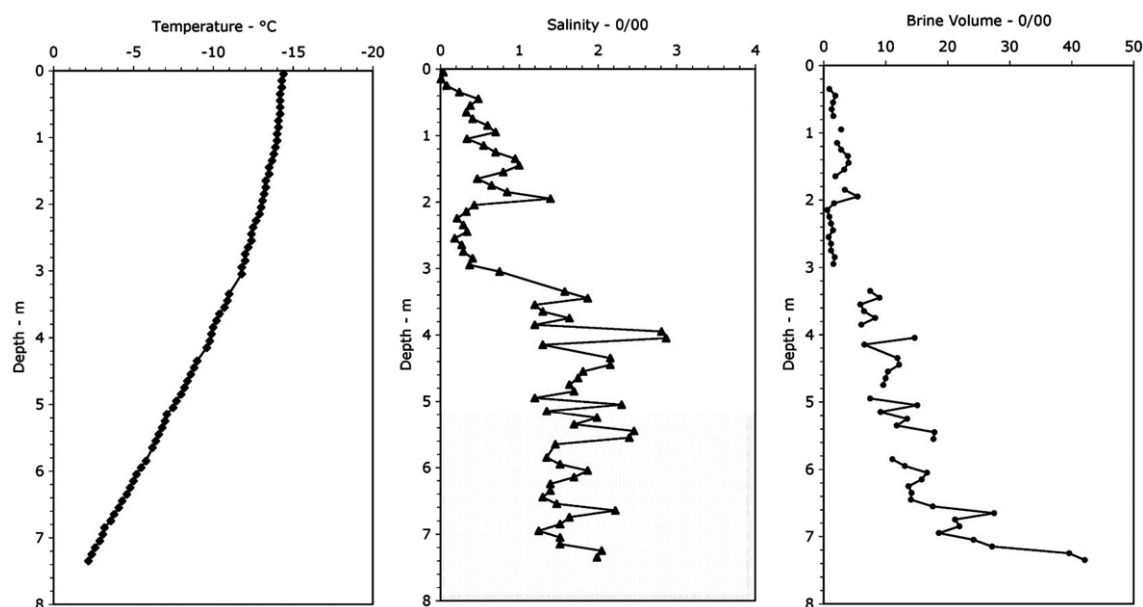


Fig. 4. Sea ice properties obtained from a multiyear ridge used in simulations for a 7.35 m core from Kovacs and Morey (1986). See text for more details.

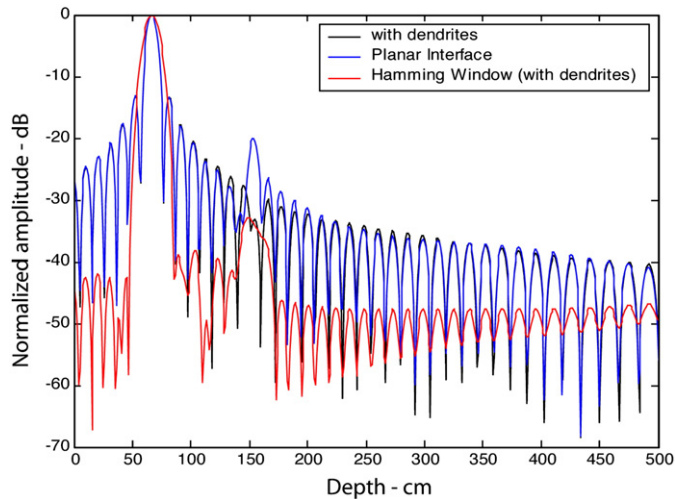


Fig. 5. Range profile simulation for 1–2 GHz penetrating radar for 0.76 m thick first-year ice with a 3 cm dendritic layer.

bandwidth available within this configuration. The Hamming window actually broadens the peaks and effectively reduces range resolution. The theoretical range resolution for this radar configuration is 75 cm hence this radar mode will not be useful for most thickness ranges of undeformed first year ice. In summary, these results (Figs. 5–7) indicate that a UHF (300–1300 MHz) radar system has both sufficient SNR and range resolution to estimate first-year sea ice thickness on the order of 1 m, while the VHF and L-band configurations are not optimal for this ice type and thickness range.

2.2.2. Multiyear ice

To study the performance of radar systems over thick multiyear ice found in the Arctic, we performed simulations using ice core properties from a 7.35 m multiyear ridge, again one of the thickest published cores we were able to locate (Kovacs and Morey, 1986) (Fig. 4). Such thickness for multiyear ice usually arises from both deformation and growth and represents a challenging scenario for depth penetration estimation, as most of the overall ice thickness distributions in the Arctic are less than 7–8 m (e.g. Vinje et al., 1998). We show the results for only the UHF and VHF systems, since lower frequencies are needed for the thicker ice, and we use only a thicker dendritic layer (5-cm thick) as the prior results showed little

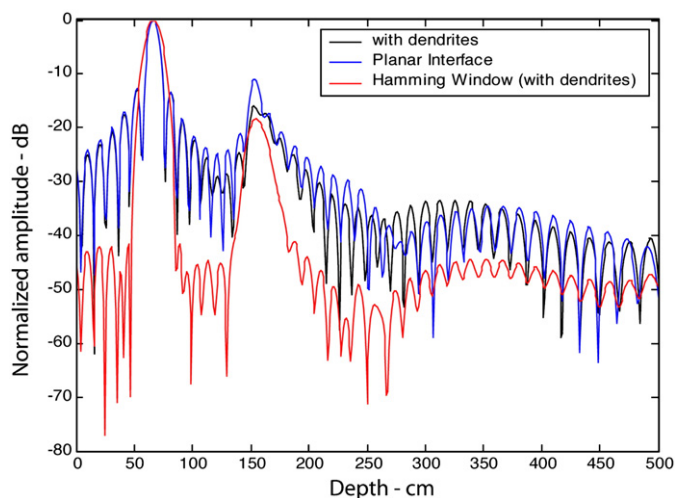


Fig. 6. Range profile simulation for a 300–1300 MHz penetrating radar for 0.76 m thick first-year ice with a 3 cm dendritic layer.

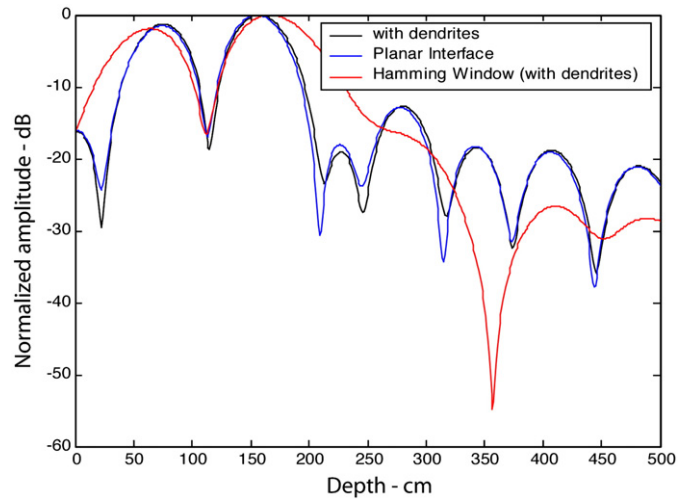


Fig. 7. Range profile simulation for a 50–250 MHz penetrating radar for 0.76 m thick first-year ice with a 3 cm dendritic layer.

sensitivity to the presence of the 3-cm layer at these lower frequencies.

Fig. 8 shows the range profile for multiyear ice obtained for the UHF (300–1300 MHz) configuration. The SNR is insufficient to clearly identify the ice–ocean interface, expected between to be located at about 8–9 m in this simulation. This is due to the propagation losses encountered by this range of frequencies as the radar waves traverse through the thick multiyear ice, which results in a significant reduction in the reflected power from the bottom interface. Sea ice has a large dielectric loss component at UHF frequencies (about 0.3–0.4 at 500 MHz, Fig. 2), which results in insufficient penetration depth of approximately 40 cm at 500 MHz (not shown) to reach the multiyear ice–ocean interface.

The same experiment was repeated using the VHF (50–250 MHz) radar system (Fig. 9). The ice–ocean interface reflection (located at about 900 cm) after application of the Hamming window is about 25 dB above the range sidelobes and is nearly as strong as the top snow–ice interface return (located at about 75 cm), indicating that the SNR is sufficient for identifying the ice–ocean interface at this depth. Further, the resolution of the VHF configuration (75 cm) is also sufficient for measuring multiyear ice thickness (usually above 2 m

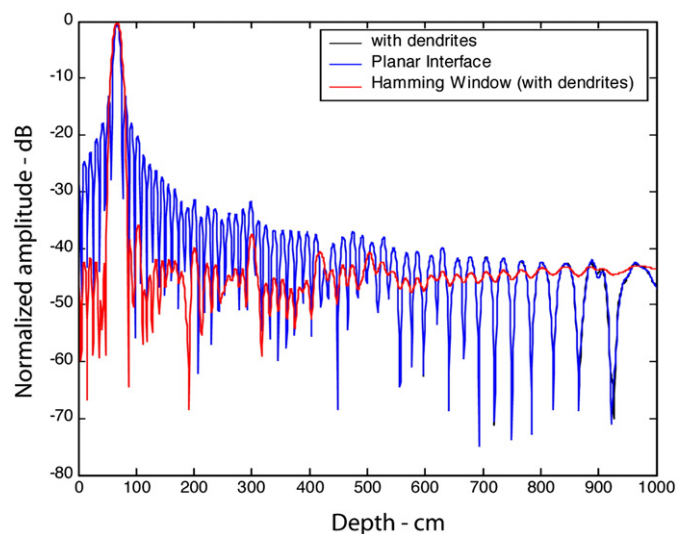


Fig. 8. Range profile simulation for a 300–1300 MHz chirp radar system over 7.35 m thick multiyear ice with a 5 cm dendritic layer.

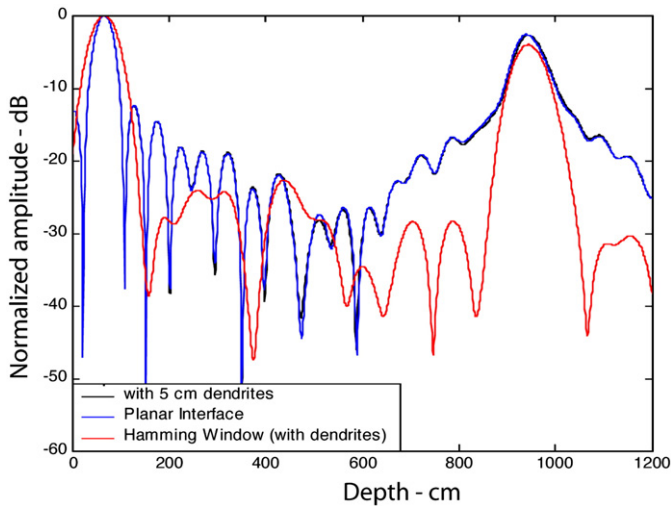


Fig. 9. Range profile simulation for a 50–250 MHz chirp radar system over 7.35 m thick multiyear ice with a 5 cm dendritic layer.

thick). There is no impact from the addition of the 5 cm dendritic layer in either the UHF or VHF configurations. Thus a VHF (50–250 MHz) radar system has both sufficient SNR and satisfactory range resolution to estimate sea ice thickness over thick multiyear ice. We expect the VHF configuration to be adequate for deformed first-year ice as well, but with reduced performance and penetration due to increased salinity and hence larger dielectric loss factor.

2.2.3. Loss with respect to frequency

We performed a loss analysis with respect to frequency at the ice–ocean interface in the 50–500 MHz range to measure the contributions of various frequencies to the overall return response for the 7.35 m multiyear ice properties (Fig. 10A). We isolated the reflection from the ice–ocean interface and performed a Fast Fourier Transform on the reflection, to measure the return power as a function of frequency. The low frequency components incur the least amount of attenuation and hence represent most of the reflected energy from the ice–ocean interface. The high frequency components suffer a significant amount of attenuation. A similar analysis was run based on the 1.22 m first-year ice properties (Fig. 10B). There is overall less attenuation at all frequencies but most particularly at the higher frequencies, as compared to Fig. 10A. These results further indicate that lower frequencies are required for thicker ice while higher frequencies are suitable for thinner ice.

2.2.4. Summary of simulations

The following inferences can be drawn from the simulation results. At the higher range of radar frequencies examined here, the presence of the dendritic interface provides a smooth impedance match between the sea ice and seawater layers that reduces the reflected energy from this interface and hence reduces the sensitivity of a penetrating radar. Overall, an ultrawideband radar system is essential for preserving the range resolution of the system, to capture returns from the snow–ice interface, to sample a wide range of ice thicknesses, and to reduce the effect of range sidelobes in masking the return from ice–ocean interface. We conclude the following: 1) VHF frequencies are suitable for sea ice penetrating radars since the dielectric loss is low at these frequencies; 2) VHF frequencies with narrow bandwidths do not have sufficient range resolution to resolve the two major ice interfaces (the snow–ice interface and the ice–ocean interface). To achieve higher range resolution, a radar system with a very high percentage bandwidth (or ultrawideband) must be used; 3) Since most of the reflected energy from the ice bottom interface comes from lower frequencies, the use of windowing such as a Hamming window

reduces range sidelobes by more than 50 dB, so that sidelobes of a strong surface return do not mask returns from the ice–ocean interface. Among the sea-ice penetrating radar configurations considered in this study, the system that operated in the 300–1300 MHz frequency range showed the best performance over first year ice (0.7 and 1.2 m), and the radar system that operated in the 50–250 MHz frequency range showed the best performance over multiyear ice (7.35 m).

3. System design and implementation

Based on the simulation results, we designed a prototype radar system operating in the frequency-modulated continuous wave (FM-CW) mode to generate the two desired modes. To reduce cost and development time, we used a modified version of a 500–2000 MHz FM-CW radar that was developed at the Radar Systems and Remote Sensing Laboratory at the University of Kansas to map near-surface internal layers over the Greenland ice sheet as a means to estimate the accumulation rate (Kanagaratnam et al., 2001, 2004). An FM-CW radar repetitively transmits a waveform where the frequency continually increases, allowing a wide bandwidth to be transmitted and enabling a high range resolution. The return signal from the target is then compared with the transmitted signal to extract the target's range, amplitude, and phase information. The difference between the transmitted signal and return signal is called the intermediate frequency (IF) and has a comparatively narrow bandwidth. This

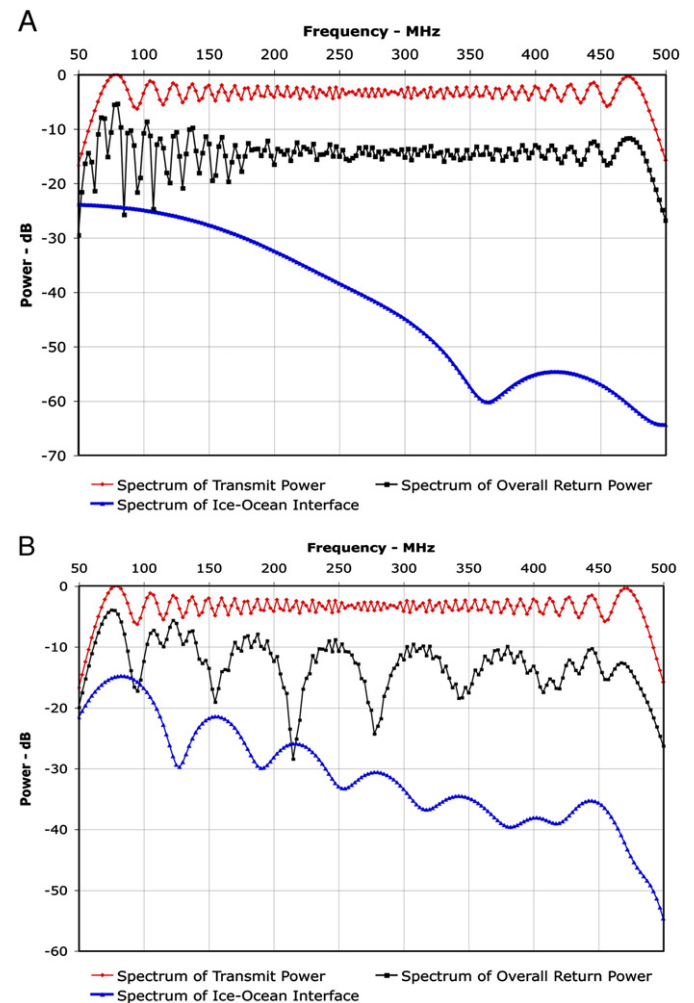


Fig. 10. Return power loss vs. frequency simulation for the ice–ocean interface from 50–500 MHz for (A) multiyear ice 7.35 m and (B) first-year ice 1.22 m model data.

capability makes it simpler to digitize the IF signal with analog-to-digital (A/D) converters operating at a lower sampling frequency instead of needing fast A/D converters as required with impulse or short-pulse radars.

One of the major challenges faced by earlier systems was the non-linear wideband sources. This resulted in less than optimum spectral response that made it difficult to identify the reflecting interfaces. However, with the advent of wireless communication over the last decade it has now become economical to develop highly sensitive wideband coherent radars. In particular, we utilized phase-lock-loop and frequency synthesizer chips to obtain a highly linear frequency sweep from a traditional Yttrium Iron Garnet (YIG) oscillator. These improvements contribute to a system with low range sidelobes and the shaping of the amplitude spectrum to reduce ringing, a noise source from re-radiation of currents within the antenna and possibly structure.

Fig. 11 shows the block diagram of the prototype FM-CW penetrating radar system with two modes of operation: a low-frequency mode over the frequency range from 50 to 250 MHz; and a high-frequency mode over the frequency range from 300 to 1300 MHz. The wide bandwidth for each mode provided adequate vertical thickness resolutions of 75 cm for the low-frequency mode and 15 cm for the high frequency mode. We note that a range of 25 cm thickness resolution or better is the basic scientific measurement goal, however the coarser resolution of 75 cm was deemed adequate for this initial feasibility test. Table 1 summarizes the radar system parameters described in more detail below.

3.1. Transmitter

We used a YIG oscillator in a Phase Locked Loop (PLL) configuration to enable the system to generate a linear chirp signal in the 4–6 GHz

frequency range. The PLL used a highly linear digital chirp synthesizer (DCS) as a reference signal to generate a linear frequency sweep with the YIG oscillator. The system can generate a highly linear frequency signal from 50 MHz to 1300 MHz by down-converting the 4–6 GHz chirp signal with a 4-GHz Phase Locked Oscillator (PLO). To generate the 50–250 MHz chirp, we down-converted a 4.05–4.25 GHz chirp from the YIG with the 4 GHz PLO. Similarly the 300–1300 MHz chirp was generated by down converting a 4.3–5.3 GHz signal from the YIG source. We used digitally controlled filters to select the desired frequency band. The signal is then passed through an automatic-gain-control (AGC) section to ensure that the signal has uniform power at all frequencies to within ± 1 dB. The AGC chain includes the power amplifier where the signal is amplified to 20 dBm. A portion of this signal is then tapped with a directional coupler to serve as a local oscillator in the receiver. The rest of the signal is filtered again to suppress harmonics that were generated by the amplifiers. Finally, the signal is attenuated by 3 dB and transmitted. The attenuator reduced any mismatch between the amplifier and the antenna.

3.2. Receiver

At the receiver, we used a low-gain, high-isolation amplifier to provide about a 10 dB gain to the received signal before mixing it with the reference signal. The high-isolation amplifier provides 50 dB of isolation. This is crucial in suppressing the LO signal that would otherwise be coupled to the RF-port of the mixer and radiated via the receive antenna. We used attenuators in the receive chain to reduce the mismatch between the antenna and amplifier, and the amplifier and mixer. We then high-pass filtered the intermediate frequency (IF) output from the mixer to suppress the direct leakage signal from the transmit antenna to the receive antenna. Finally, the signal is low-pass filtered and digitized at 500 kHz before storage.

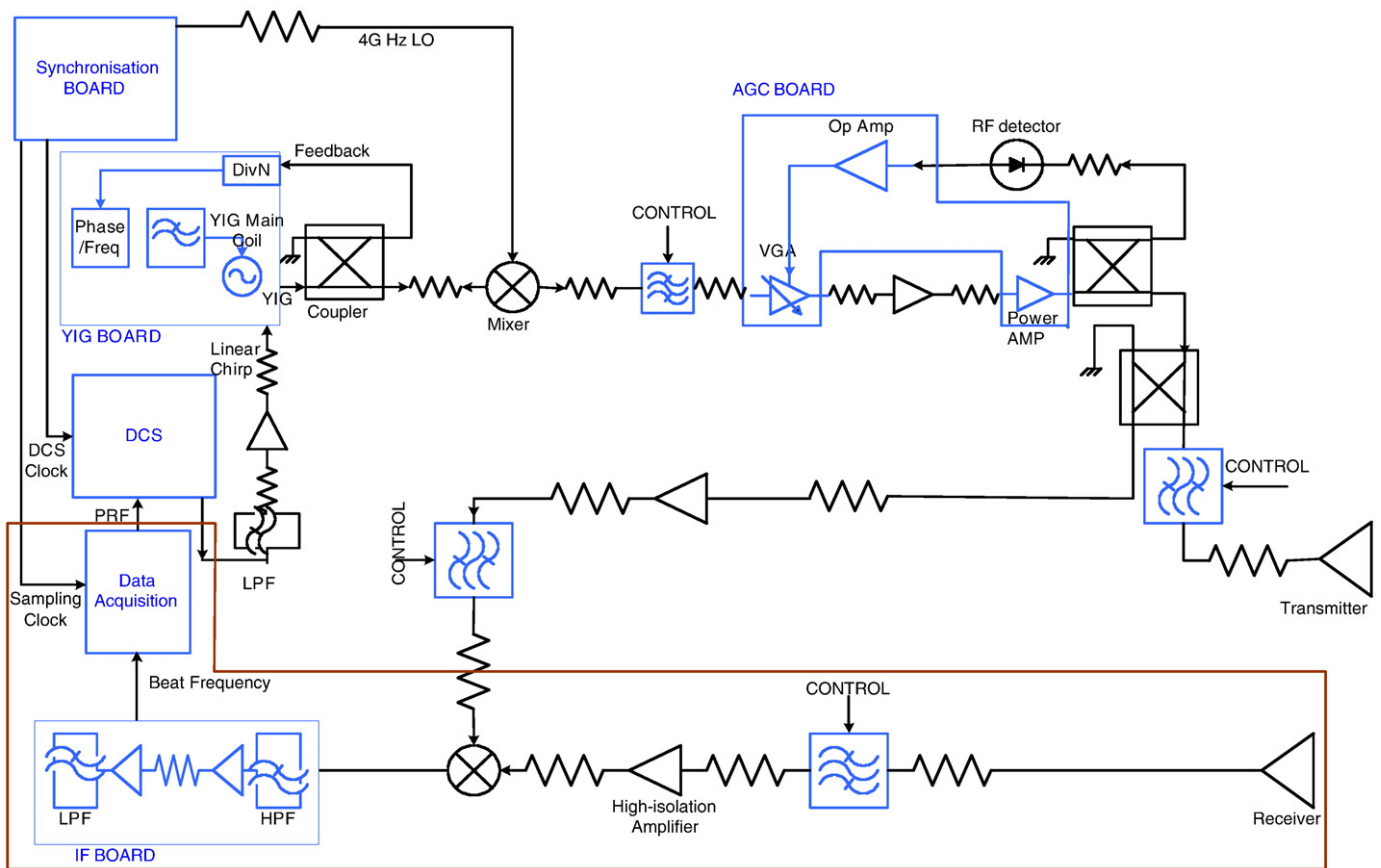


Fig. 11. Block diagram of sea ice thickness radar system. The receiver component is outlined in brown while the transmitter constitutes the remainder of the diagram.

3.3. Antennas

We developed two sets of bowtie antennas with rounded edges (Birch and Palmer, 2002) for the two frequency modes. The antennas were driven with a 3:1 RF transformer balun and terminated with a 250 Ω resistor at the edge of the antenna. The effects of antenna ringing from the direct leakage signal had the potential to mask the weak returns that are expected from the sea-ice/water interface. The resistor termination helped to dampen the ringing quickly and thus makes the radar more sensitive to the weaker returns. The bowtie antennas operating at 50–250 MHz had a length of 80 cm while the antennas operating at 300–1300 MHz had a length of 20 cm. We used simple dipole antennas for the 50–250 MHz band and a four-element dipole array for the 300–1300 MHz band. Each mode consisted of separate transmit and receive antennas. The beam pattern of a dipole antenna on a dielectric medium has been investigated extensively (Compton et al., 1987). Since the return signal is dominated by a quasi-specular return, the reflected signal is determined by one Fresnel zone, which is about 2.5 m for 10 m thick ice at 150 MHz.

The antennas were enclosed in a plexiglass cavity, formed as a sled, to prevent back-radiation (Fig. 12A). The antennas were installed at the bottom of the sled, which was made of 1.25 mm thick plexiglass and enclosed both pairs of antennas. The radar sled measured about 2 m in length and 1 m in width, with the radar system, 12-volt batteries, and operating computer placed on top of the enclosed sled (Fig. 12B). A snow machine then towed the radar sled across the ice for sampling (Fig. 12C). We estimate that the system and sled together weighed approximately 70–80 kg.

3.4. Data collection and post-processing

The received signal data was processed using a 12-bit A/D converter at a sampling rate of 50 MHz and then decimated to reduce the sampling rate to 5 MHz. The transmitter signal was linearly-frequency modulated at a rate of 100 Hz. The signal processing consisted of conditioning the data to reduce DC offsets followed by integration and deconvolution to reduce system effects. A Hamming window was utilized, as in the model development, to reduce sidelobes in the frequency domain. The data were then Fourier transformed to obtain range profiles. For the initial computations of the stationary measurements, a single propagation speed of 1.73e8 m/s was used to convert the two-way propagation time through the ice into thickness. This speed was determined based on modeling results described earlier for approximately 1 m thick cold first-year ice. The propagation speed will vary with salinity and temperature and the subsequent estimated dielectric constant and attenuation loss. Refinements to processing would include the use of properties derived from nearby ice cores to recalculate these parameters.

4. Results of sea ice field tests

We conducted two field tests of the penetrating radar, both of which included coincident collection of in situ measurements to evaluate the radar's performance. The initial test took place off Barrow, Alaska, between April 27 and May 5, 2003, using the low-frequency mode only. The second test was performed off East Antarctica during October 2003, where both the low- and high-frequency modes were evaluated.

4.1. Results from the Alaska field test

The Alaska field test was conducted over landfast first-year ice, which is readily accessible from the shore adjacent to Barrow. In this region, landfast ice is composed of expanses of undeformed ice separated by deformed ice, where the latter either drifts toward the coast from offshore or is formed in situ when drifting pack ice

converges upon the coast (Mahoney et al., 2007). Similarly, the level ice may be advected from offshore or form in place. A detachment event moves landfast ice offshore, which reduces the landfast ice area and leaves open water at the landfast ice edge. As a result of successive detachment and convergence events, there can be a variety of different thicknesses of level ice between ridges. A snow machine towed the radar along three 200 m long ice transects. The transects were established to capture varying thicknesses of undeformed ice and some deformed thicker ice which was navigable by the sled. No multiyear ice was observed in this region during the experiment.



Fig. 12. Radar system showing A) one pair of low frequency and high frequency mode bowtie antennas within plexiglass sled; B) complete radar system with antennas within enclosed sled and the radar system, battery, and computer on top of sled; C) radar sled being towed by snow machine across landfast ice off Barrow, Alaska.

4.1.1. Sea ice properties

The first-year ice thickness along the three transects ranged from approximately 0.5 m to greater than 4 m. Along each transect adja-

cent to the radar track, ice auger drill holes were obtained every 20 m at the stationary radar measurement points. A 10-cm diameter ice core was obtained for each transect from which in-situ temperature

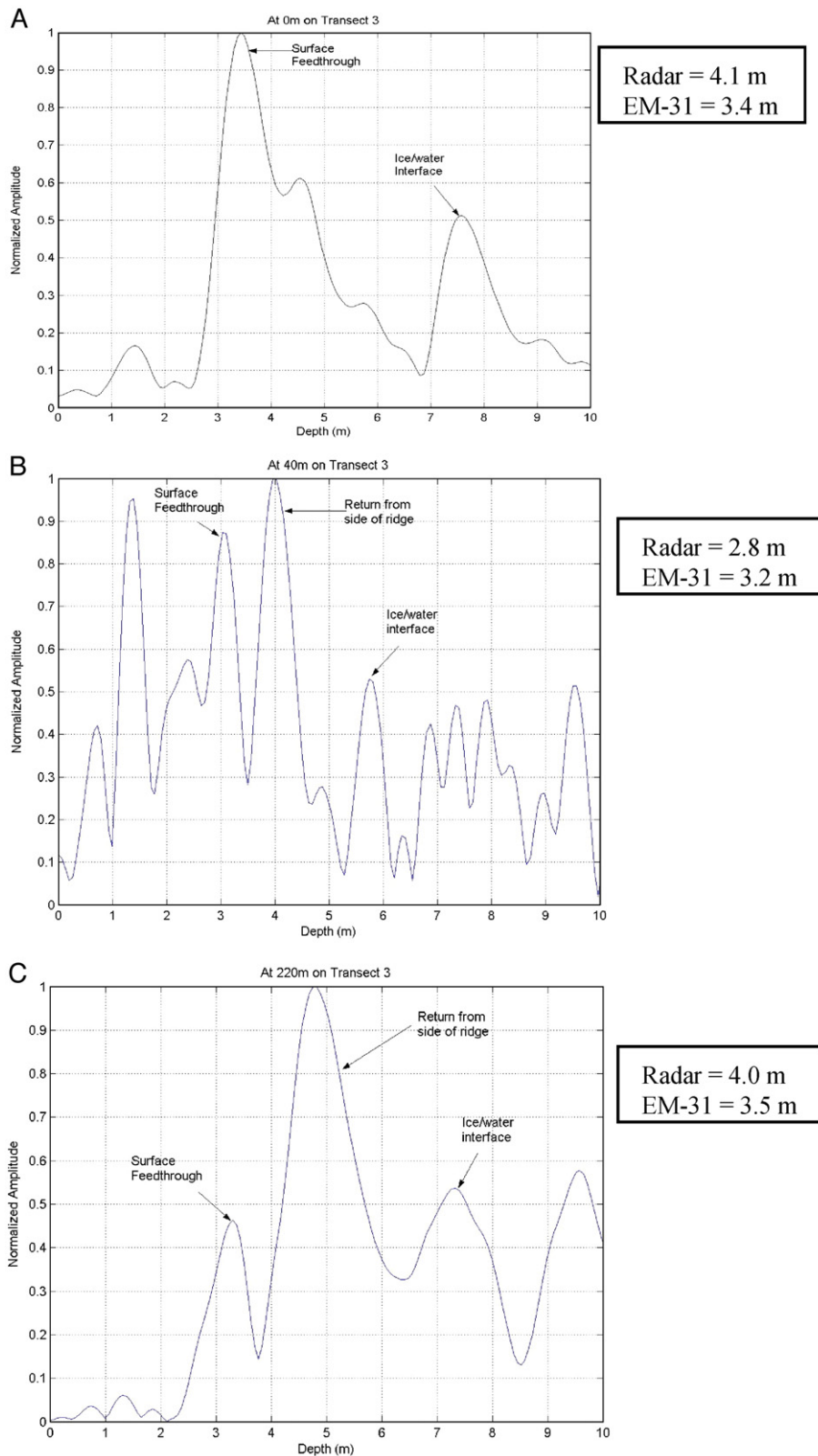


Fig. 13. Sample radar returns off Barrow obtained May 4, 2003 at distances of A) 0 m, B) 40 m, and C) 220 m along transect 3 and the associated EM-31 thickness measurements. The peaks of the top and bottom ice surfaces are identified. Also identified in B) and C) are peaks thought to arise from the side of ridges or sloping ice, more clearly identified in Fig. 14.

and salinity profiles were taken. The electromagnetic (EM) conductivity measurements were made using a Geonics EM-31 device in horizontal dipole mode placed on a sled, which operated at a frequency of 9.8 kHz with a 3.66 m coil separation. Both EM and snow depth measurements were made every 4 m along each transect. The ice and EM in situ measurements are described more thoroughly in Mahoney (2003).

Transects 1 and 2 both started on undeformed ice and moved into areas of thicker ice with small-scale surface roughness on the order of a few centimeters, with ice cores of length 1.4 m taken near the start of both transects. Transect 3 took advantage of a trail cut through small ridges by Inupiat whaling crews, thereby allowing the radar sled to travel over two regions of ice substantially thicker than along transects 1 and 2. In many places the ice was thicker than 4 m, which was unfortunately the maximum length of the ice auger that we carried at the time, and so two drill hole measurements made at 0 m and 220 m along transect 3 did not extend completely through the ice. These two depth-limited auger measurements provide some additional interpretation of the radar data (see below) but are not included in any statistical analysis. The core for transect 3 was taken in ice thicker than 4 m and only the top 1 m was recoverable. The top 5–10 cm of the three cores was composed of granular frazil ice with the remainder of each core composed primarily of columnar ice. The three ice cores had bulk salinities in the range of 3.5–8 psu and temperatures between -3 and -7 °C, with the coldest ice temperatures obtained during transect 3 when the air temperatures were less than -6 °C (May 4). Mean snow depths from the three transects were between 10 and 14 cm, with standard deviations of 8–9 cm.

Along transect 3 obtained on May 4, where the greatest proportion of deformed ice was crossed, the auger encountered several voids, detected by feeling the auger drop suddenly as it drilled through the sea ice. We encountered voids at 0 m, 40 m, and 220 m along the transect, within the thickest ice encountered by the radar. Although it was difficult to measure the upper and lower positions of the ice voids, we estimated that the voids encountered were <10 cm deep. Typically, where the auger encountered voids, there were multiple voids, suggesting rubble ice or many layers of rafted ice. Some voids were dry while others contained water. A dry cavity was found approximately 3 m from the surface 40 m along transect 3, suggesting at least 3 m of freeboard and therefore a considerable thickness of ice (>12 m, assuming a conservative keel:sail ratio of 4:1).

The footprint of the EM-31 is on the order of the coil spacing (3.66 m). Final EM thickness measurements are based on estimates of sea ice conductivity calculated from the in situ data. We used a 1-dimensional (1-D) conductivity model described by Haas et al. (1997) and Haas and Eicken (2001) to derive thickness. In general, 1-D EM model estimates compare quite well with measurements over uniform level ice, but when ice thickness is changing, including over ridges or underlying keels and over thin ice (5–20 cm) in the vicinity of thicker ice, the EM measurements may either underestimate or overestimate thickness, respectively. The summary of many studies (both airborne and surface) show that the EM technique has a thickness precision of about 0.1–0.2 m and accuracy on the order of 5% for ice between 1 and 6 m thick (e.g. Haas, 2003; Kovacs and Holladay, 1990; Multala et al., 1996). The complex distribution of ice and voids of seawater and air, particularly such as found along transect 3, underlines the inadequacy of the assumption of uniform sea ice conductivity used for the EM conductivity estimates. Sensitivity studies using different thicknesses of seawater in voids showed that the presence of seawater within an ice cover resulted in an underestimation of thickness by the EM of up to 20% for 4 m ice (Mahoney, 2003). The mean difference between the auger and EM calculations is 2 cm with a standard deviation of 22 cm, values within the range of published EM accuracies noted above. These results indicate that the EM thickness data are useful for validation with the radar measurements.

4.1.2. Radar measurement results

Quantitative low frequency radar data were obtained at stationary points along the entire length of transect 3 as well as a limited portion of transect 2. Fig. 13 shows sample radar returns obtained at 0, 40, and 220 m along transect 3, with the complete set of radar, EM, and auger results for this transect shown in Fig. 14. The radar scopes in Fig. 13 indicate clearly identifiable peaks from the snow–ice (surface feedthrough) and ice–ocean surfaces. The sites at 0 and 220 m were noted to have water-filled voids. Also seen in Fig. 13B (40 m) and c (220 m) are strong intermediate peak returns that are likely coming from the sides of keels, which are readily identifiable in Fig. 14. We do not have a ready explanation for the initial strong peak before the snow–ice peak in Fig. 13B, except to note that a dry cavity was identified by the auger at about 3 m depth as described previously which may account for the early return.

The results in Fig. 14 show that the radar returns respond to varying thicknesses. The differences between the point source auger measurements and the wider-beam radar measurements at each 20 m may simply be due to area sampled, i.e. the auger measures a point while the radar beam detects a broader area than the auger and is thus likely sampling a more variable range of thicknesses. We cannot account for the large discrepancy found at 180 m between the radar and both the auger and EM measurements, at least in terms of ice properties as the ice thickness nearby appears to be comparatively uniform. At 0 m and 220 m, the EM measurements are about 0.5 m less than the radar values (see also Fig. 13A and B), which may be due to the previously noted presence of water-filled voids resulting in an underestimation of the EM values. This possible underestimation of the EM values is further emphasized by two incomplete auger measurements noted above at these two same locations, where the ice thickness is at least 4 m thick, with the auger measurements being limited to 4 m due to a lack of additional extensions.

In a limited test of the model based on field data, we used the measured sea ice properties derived from the ice core obtained for transect 2 at 60 m along the transect to recalculate the dielectric constant, attenuation loss and velocity of propagation. For the low-frequency mode, the radar obtained a thickness of 1.9 m, while the simulation result was about 1.5 m. For the same location, the auger measurement was 1.45 m while the EM measured 1.35 m. These observations were made from a relatively uniform portion of undeformed ice.

4.2. Results from the Antarctic tests

Additional radar experiments were conducted as a part of the AMSR-E sea-ice validation ship-based experiments in East Antarctica

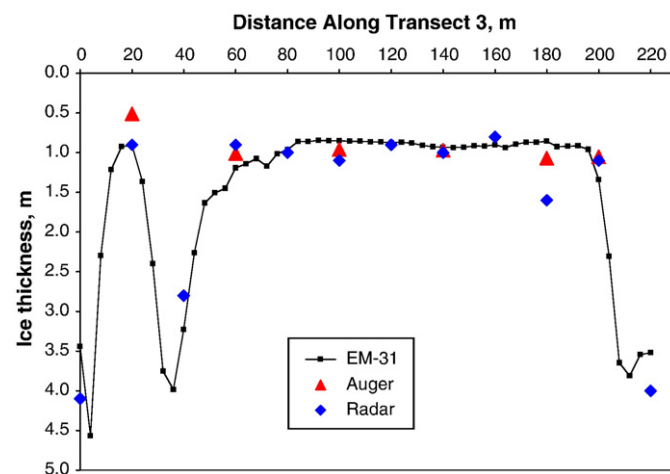


Fig. 14. A comparison of ice thickness measurements obtained by penetrating radar, EM-31, and ice auger along transect 3, May 4, 2003.

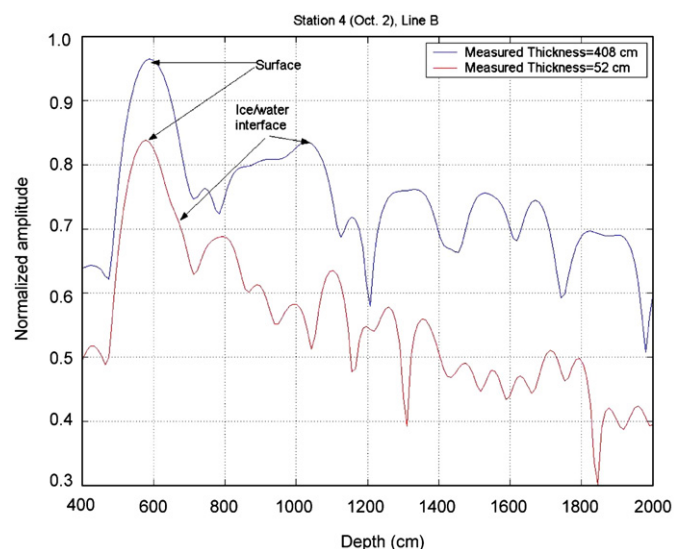


Fig. 15. Sea ice thickness measurements from Antarctica obtained October 2, 2003 in the low frequency (50–250 MHz) mode.

during September–October 2003 (Massom et al., 2006). Both the high- and low-frequency modes were evaluated. The high-frequency antennas were mounted in the base of a snow-thickness radar sled (Kanagaratnam et al., 2007) and the low-frequency radar antennas were mounted under the base of a second sled, a revised sled configuration from the Barrow test. Sea-ice thickness measurements were collected at stationary points every 5 m along a transect and also with the sleds moving continuously along the transect line. While extensive data were collected in each mode, only a few samples have been processed to date. Data on sea-ice temperature, salinity and crystal structure were also collected from core samples along each transect.

We show two examples of radar returns from stationary measurements over ice of different thickness obtained in both modes. In the low-frequency mode, measured ice of 4.08 m resulted in clearly defined peaks from the top and bottom ice surfaces, with a

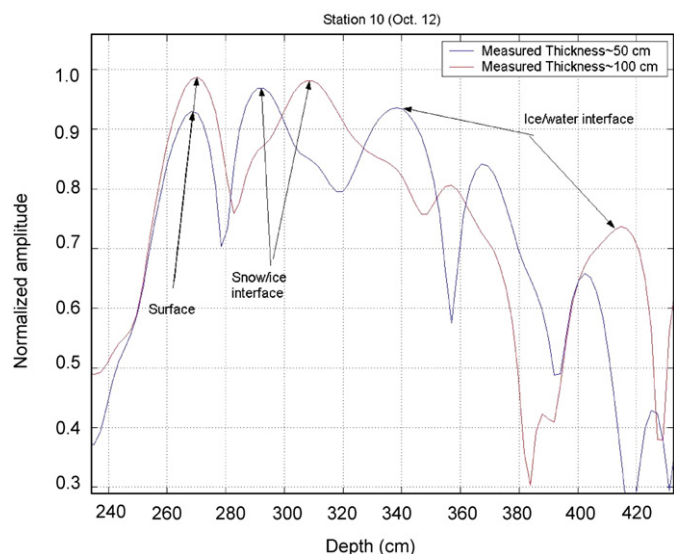


Fig. 16. Sea ice thickness measurements from Antarctica obtained October 12, 2003 in the high frequency (300–1300 MHz) mode.

radar result of about 4.3 m (Fig. 15). Also shown is a trace over thinner ice that is about 50 cm thick, which is thinner than its vertical resolution of 75 cm, with only the peak from the top ice surface clearly resolved. In the high-frequency mode (Fig. 16), which has a vertical resolution of about 15 cm, clearly detectable peaks measuring about 45 and 105 cm in thickness agree well with the auger measurements of 50 and 100 cm. We can also see that the high-frequency radar is also able to map snow thicknesses of about 20 and 40 cm, shown here between the air–snow interface and the snow–ice interface, using similar methodology but different range of frequencies as described in Kanagaratnam et al. (2007).

4.3. Summary of results

In Fig. 17 we show the differences in thickness measurement between the radar compared to both the EM and auger data for all available measurements. For Barrow, this includes two points from transect 2 and all points from transect 3, but does not include the two depth-limited auger measurements at 0 and 220 m. For Antarctica, we include the three radar–auger observations from Figs. 15 and 16. The R^2 correlation values for the auger–radar comparisons are higher (0.96) than for the EM–radar comparisons (0.90). For the auger–radar comparisons, the mean difference is 16 cm with a standard deviation of 21 cm, based on 11 data points. For the EM–radar comparisons, the mean difference is 13 cm with a higher standard deviation of 36 cm, based on 14 data points. Combining the two sets of measurements

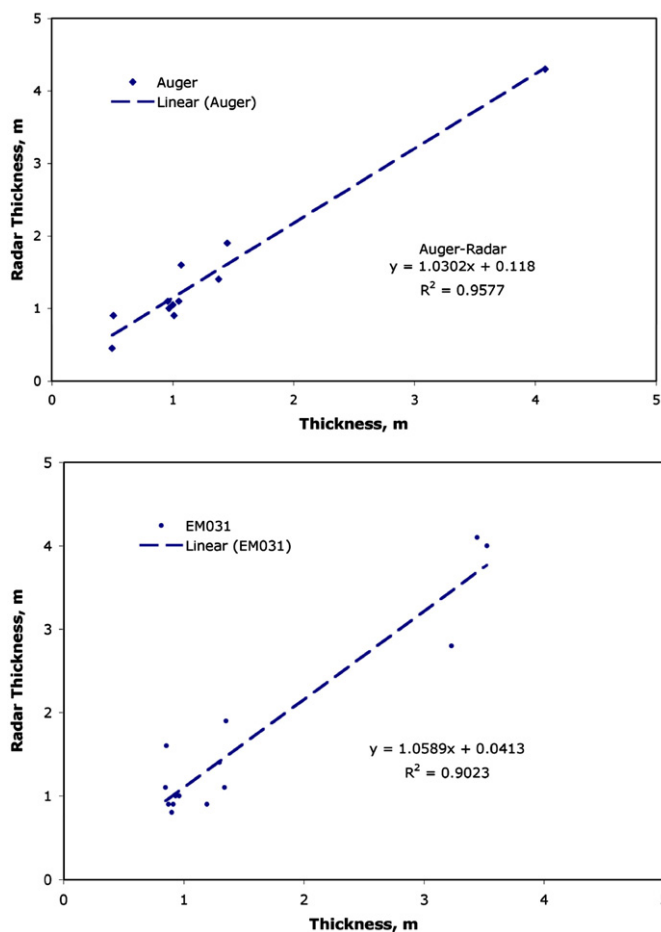


Fig. 17. Comparison of thickness measurements made by auger (top) and EM-31 (bottom) with penetrating radar, including results from both transects 2 and 3 off Barrow and from Antarctica (Figs. 15 and 16).

results in an overall mean difference of 14 cm and a standard deviation of 30 cm (total 25 points).

From both sets of returns shown in Figs. 13, 15, and 16, the comparative amplitudes of the returns from the snow–ice and ice–ocean interfaces can vary quite a lot, with complexity added apparently from nearby ridges. The differences are mostly likely due to variations in internal ice properties, including ice temperature and salinity, and the presence of voids and discontinuities, and other parameters not yet included in the modeling effort such as surface roughness, all in relation to the utilized modes and range of frequencies.

5. Discussion

Based on the initial tests described above, we have demonstrated the potential of using ultrawideband radar for measuring first-year sea ice that ranged between 0.5 and 4 m thick, with mean differences of about 15 cm compared to auger and EM measurements. These results were done using both the low frequency (50–250 MHz) and high frequency (300–1300 MHz) modes as a means to extend the measurement thickness range. The system was designed to measure sea ice between 30 cm and 7 m thick, and we believe that a greater thickness is achievable up to at least 10 m. More field evaluations of course are needed over multiyear and deformed ice, including over ice thicknesses greater than 7 m, to fully demonstrate the capability of this concept. Careful in situ observations of ice thickness, internal discontinuities and other properties including roughness are necessary to more completely model and understand the radar returns. The ability to detect the snow–ice and ice–ocean interfaces as a means to measure thickness, particularly for the thicker components of the ice thickness distribution, would represent considerable improvement over the current capabilities of both surface- and helicopter-based EM instruments.

Several modifications are needed to improve this radar system. A single operating mode and antenna system with a frequency range of 100–1200 MHz would result in an overall system thickness resolution of about 15 cm and accommodate the entire thickness measurement range goals of the system. Other modifications include the optimization of the ultrawideband antenna performance to cover the entire frequency range and a system that could operate from a low-flying airborne platform including a robotic plane. We have already developed techniques to deconvolve the system response based on impulse response measurements over calm ocean. This will further increase the airborne system's sensitivity by removing the system imperfections. The addition of top and bottom surface roughness parameters, preferred dendrite layer orientation, snow depth and properties, and the inclusion of wet and dry voids would significantly enhance the modeling effort and understanding of the radar returns. Moving to an airborne platform would also require a method to sharpen the beam to maintain satisfactory horizontal resolution. This could be done by the use of multiple antennas and synthetic aperture radar processing techniques. An airborne instrument would not be subject to ionospheric effects with the low-frequency ranges being utilized, as would an equivalent spaceborne system. The airborne capability could be utilized in conjunction with field programs and as validation for satellite observations of proxy or indirect measurements of sea ice thickness. The inclusion of a snow thickness radar (Kanagaratnam et al., 2007) would enable a more complete description of the ice cover and enable heat flux estimates. Placing such an instrument on a robotic plane would potentially extend the observation sampling duration and area significantly compared to an airplane. With sufficient understanding and verification of the radar thickness observations, such an instrument could be utilized to validate sea ice thickness estimates obtained by spaceborne laser and radar altimetry missions.

Acknowledgements

This work was supported by the California Institute of Technology President's Fund with additional support provided by the National Aeronautics and Space Administration through a contract with the Jet Propulsion Laboratory, California Institute of Technology. We thank Hajo Eicken of the University of Alaska Fairbanks for providing the in situ instrumentation used in the Alaska field test, Saikiran Namburi and Krishna Gurumoorthy of the University of Kansas for instrument development and field support, Glenn Sheehan and Matthew Irinaga of the Barrow Arctic Research Consortium for logistical support, and Brandon Heavey of the Jet Propulsion Laboratory for the helpful comments.

References

- ACIA, 2005. Arctic Climate Impact Assessment. Cambridge University Press, New York City, New York, p. 1042.
- Birch, M., Palmer, K.D., 2002. An optimized bowtie antenna for pulsed low frequency ground penetrating radar. *Proc. SPIE* 4758, 573–578.
- Compton, R.C., McPhedran, R.C., Popovic, Z., Rebeiz, G.M., Tong, P.P., Rutledge, D.B., 1987. Bow-tie antennas on a dielectric half-space: theory and experiment. *IEEE Trans. Antennas Propag.* 35, 622–631.
- Cox, G.F.N., Weeks, W.F., 1983. Equations for determining the gas and brine volumes in sea ice samples. *J. Glaciol.* 29 (102), 306–316.
- Cox, G.F.N., Weeks, W.F., 1988. Profile properties of undeformed first-year sea ice, CRREL Report 88-13. U.S. Army Cold Regions and Engineering Laboratory, Hanover, N.H.
- Debye, P., 1929. *Polar Molecules*. Dover, New York.
- Elachi, C., 1987. *Introduction to the Physics and Techniques of Remote Sensing*. Wiley and Sons, p. 413.
- Forsberg, R., Skourup, H., 2005. Arctic Ocean gravity, geoid and sea–ice freeboard heights from ICESat and GRACE. *Geophys. Res. Lett.* 32. doi:10.1029/2005GL023711.
- Goff, J.A., Stewart, W.K., Singh, H., Tang, X., 1995. Quantitative analysis of sea ice draft. 2. Application of stochastic modeling to intersecting topographic profiles. *J. Geophys. Res.* 100 (C4), 7005–7017.
- Haas, C., 1998. Evaluation of ship-based electromagnetic-inductive thickness measurements of summer sea-ice in the Bellinghousen and Amundsen Seas, Antarctica. *Cold Reg. Sci. Technol.* 27, 1–16.
- Haas, C., 2003. Dynamics versus thermodynamics: the sea ice thickness distribution. In: Thomas, D.N., Dieckmann, G.S. (Eds.), *Sea Ice: An Introduction to its Physics, Chemistry, and Biology, and Geology*. Blackwell, pp. 82–112.
- Haas, C., Eicken, H., 2001. Interannual variability of summer sea ice thickness in the Siberian and Central Arctic under different atmospheric circulation regimes. *J. Geophys. Res.* 106, 4449–4462.
- Haas, C., Gerland, S., Eicken, H., Miller, H., 1997. Comparison of sea–ice thickness measurements under summer and winter conditions in the Arctic using a small electromagnetic induction device. *Geophysics* 62, 749–757.
- Hallikainen, M., Winebrenner, D.P., 1992. The physical basis for sea ice remote sensing. In: Carsey, F. (Ed.), *Microwave Remote Sensing of Sea Ice*. Geophysical Monograph, vol. 68. Amer. Geophys. Un., pp. 29–46.
- Integrated Global Observing Strategy, 2007. Cryosphere Theme Report. World Meteorological Organization. WMO/TD-No. 1405, August 2007, 100 pp. Available from <http://igos-cryosphere.org>.
- Intergovernmental Panel on Climate Change (IPCC), 2007. Fourth Assessment Report, Climate Change 2007: Synthesis Report. 23pp. Available from <http://www.ipcc.ch/index.htm>.
- Izuka, K., Freundorfer, A.P., Wu, K.H., Mori, H., Ogura, H., Nguyen, V.K., 1984. Step-frequency radar. *J. Appl. Phys.* 56 (9), 2572–2583.
- Kanagaratnam, P., Gogineni, S.P., Gundestrup, N., Larsen, L., 2001. High-resolution radar mapping of internal layers at the North Greenland ice core project. *J. Geophys. Res.* 106 (D24), 33,799–33,812.
- Kanagaratnam, P., Gogineni, S.P., Ramasami, V., Braaten, D., 2004. A wideband radar for high-resolution mapping of near-surface internal layers in glacial ice. *Trans. Geosci. Remote Sens.* 42 (3), 483–490.
- Kanagaratnam, P., Markus, T., Lytle, V., Heavey, B., Jansen, P., Prescott, G., Gogineni, S.P., 2007. Ultrawideband radar measurements of thickness of snow over sea ice. *Trans. Geosci. Remote Sens.* 45 (9), 2715–2724.
- Kong, J.A., 1986. *Electromagnetic Wave Theory*. John Wiley & Sons, New York.
- Kovacs, A., Morey, R.M., 1979. Anisotropic properties of sea ice in the 50- to 150-MHz range. *J. Geophys. Res.* 84 (C9), 5749–5759.
- Kovacs, A., Morey, R.M., 1986. Electromagnetic measurements of multi-year sea ice using impulse radar. *Cold Reg. Sci. Tech.* 12, 67–93.
- Kovacs, A.D., Holladay, J.S., 1990. Sea–ice thickness measurements using a small airborne electromagnetic induction system. *Geophysics* 55, 1327–1337.
- Kovacs, A., Morey, R.M., Cox, G.F.N., Valteau, N.C., 1987a. Electromagnetic property trends in sea ice, Part 1. CRREL Report 87-6, U.S. Army Cold Regions and Engineering Laboratory, Hanover, N.H.
- Kovacs, A., Morey, R.M., Cox, G.F.N., 1987b. Modeling the electromagnetic property trends in sea ice, Part 1 Cold Regions. *Sci. Tech.* 14, 207–235.
- Kwok, R., 2007. Near zero replenishment of the Arctic multiyear sea ice cover at the end of 2005 summer. *Geophys. Res. Lett.* 34 (5) Art. No. L05501.

- Kwok, R., Cunningham, G.F., Hibler III, W.D., 2003. Sub-daily sea ice motion and deformation from RADARSAT observations. *Geophys. Res. Lett.* 30 (20), 2218. doi:10.1029/2003GL018723.
- Kwok, R., Cunningham, G.F., Zwally, H.J., Yi, D., 2007. Ice, Cloud, and land Elevation Satellite (ICESat) over Arctic sea ice: Retrieval of freeboard. *J. Geophys. Res.* 112 (C12013). doi:10.1029/2006JC003978.
- Laxon, S., Peacock, N., Smith, D., 2003. High interannual variability of sea ice thickness in the Arctic region. *Nature* 425 (6961), 947–950.
- Lindsay, R.W., Zhang, J., 2005. The thinning of Arctic sea ice, 1988–2003: have we passed a tipping point? *J. Climate* 18, 4879–4894.
- Liu, J., Curry, J.A., Martinson, D.G., 2004. Interpretation of recent Antarctic sea ice variability. *Geophys. Res. Lett.* 31, L02205. doi:10.1029/2003GL018732.
- Mahoney, A., 2003. EMI measurements of ice thickness at Barrow field report. Geophysical Institute, University of Alaska Fairbanks, Fairbanks, AK. 9 pp.
- Mahoney, A., Eicken, H., Gaylord, A.G., Shapiro, L., 2007. Alaska landfast sea ice: links with bathymetry and atmospheric circulation. *J. Geophys. Res.* 112, C02001. doi:10.1029/2006JC003559.
- Manninen, A.T., 1997. Surface roughness of Baltic sea ice. *J. Geophys. Res.* 102 (C1), 1119–1139.
- Massom, R., Worby, A.P., Lytle, V., Markus, T., Allison, I., Scambos, T., Enomoto, H., Tateyama, K., Haran, T., Comiso, J., Pfaffling, A., Tamura, T., Muto, A., Kanagaratnam, P., Giles, B., Young, N., Hyland, G., 2006. ARISE (Antarctic Remote Ice Sensing Experiment) in the East 2003: validation of satellite-derived sea-ice data products. *Ann. Glaciol.* 44 (1), 288–296.
- Meier, W.N., Stroeve, J.C., Fetterer, F., Knowles, K., 2005. Reductions in Arctic sea ice no longer limited to summer. *Eos, Trans. Amer. Geophys. Union* 86 (36), 32.
- Melling, H., Riedel, D.A., Gedalof, Z., 2005. Trends in the draft and extent of seasonal pack ice, Canadian Beaufort Sea. *Geophys. Res. Lett.* 32, L24501. doi:10.1029/2005GL024483.
- Misaridis, T., Jensen, J.A., 2005. Use of modulated excitation signals in medical ultrasound. Part II: design and performance for medical imaging applications. *IEEE Trans. Ultrason. Ferroelectr. Freq. Control* 52 (2), 192–207.
- Multala, J., Hautaniemi, H., Oksama, M., Lepparanta, M., Haapala, J., Herlevi, A., Riska, K., Lensu, M., 1996. An airborne electromagnetic system on a fixed wing aircraft for sea ice thickness mapping. *Cold Reg. Sci. Tech.* 24, 355–373.
- Okamoto, K., Mineno, H., Uratsuka, S., Inomata, H., Nishio, F., 1986. Step-frequency radar for the measurement of sea ice thickness. *Mem. Natl. Inst. Polar Res., Spec. Issue* 45, 56–65.
- Richter-Menge, J., Overland, J., Proshutinsky, A., Romanovsky, V., Bengtsson, L., Brigham, L., Dyurgerov, M., Gascard, J.C., Gerland, S., Graverson, R., Haas, C., Karcher, M., Kuhry, P., Maslanik, J., Melling, H., Maslowski, W., Morison, J., Perovich, D., Przybylak, R., Rachold, V., Rigor, I., Shiklomanov, A., Stroeve, J., Walker, D., Walsh, J., 2006. State of the Arctic Report, NOAA OAR Special Report, NOAA/OAR/PMEL, Seattle, WA, p. 36.
- Rosen, P.A., Hensley, S., Joughin, I.R., Li, F.K., Madsen, S.N., Rodriguez, E., Goldstein, R.M., 2000. Synthetic aperture radar interferometry. *Proc. IEEE* 88 (3), 333–382.
- Rothrock, D.A., Zhang, J., 2005. Arctic Ocean sea ice volume: what explains its recent depletion? *J. Geophys. Res.* 110, C01002. doi:10.1029/2004JC002282.
- Rothrock, D.A., Yu, Y., Maykut, G.A., 1999. Thinning of the Arctic sea-ice cover. *Geophys. Res. Lett.* 26 (23), 3469–3472.
- Rothrock, D.A., Zhang, J., Yu, Y., 2003. The arctic ice thickness anomaly of the 1990s: a consistent view from observations and models. *J. Geophys. Res.* 108 (C3), 3038. doi:10.1029/2001JC001208.
- Stroeve, J., Holland, M.M., Meier, W., Scambos, T., Serreze, M., 2007. Arctic sea ice decline: Faster than forecast. *Geophys. Res. Lett.* 34, L09501. doi:10.1029/2007GL029703.
- Sun, B., Wen, J., He, M., Kang, J., Luo, Y., Li, Y., 2003. Sea ice thickness measurement and its underside morphology analysis using radar penetration in the Arctic Ocean. *Sci. China* 46 (11), 1151–1160.
- Thorndike, A.S., Rothrock, D.A., Maykut, G.A., Colony, R., 1975. Thickness distribution of sea ice. *J. Geophys. Res.* 80, 4501–4513.
- Thorndike, A.S., Parkinson, C., Rothrock, D.A. (Eds.), 1992. Report of the sea ice thickness workshop, 19–21 November 1991, New Carrollton, MD, available from Polar Science Center, Applied Physics Laboratory, University of Washington, Seattle WA. 98105-6698.
- Tinga, W.R., Voss, W.A.G., Blossey, D.F., 1973. Generalized approach to multiphase dielectric mixture theory. *J. Appl. Phys.* 44, 3897–3902.
- Tucker III, W.B., Perovich, D.K., Gow, A.J., Weeks, W.F., Drinkwater, M.R., 1992. Physical properties of sea ice relevant to remote sensing. In: Carsey, F. (Ed.), *Microwave Remote Sensing of Sea Ice*. AGU Geophysical Monograph, vol. 68, pp. 9–28. Chapter 2.
- U.S. National Research Council, 2001. *Enhancing NASA's Contributions to Polar Science*. National Academy Press, Washington DC, p. 124.
- Vant, M.R., Ramseier, R.O., Makios, V., 1978. The complex-dielectric constant of sea ice at frequencies in the range 0.1–40 GHz. *J. Appl. Phys.* 49 (3), 1264–1280.
- Vinje, T., Nordlund, N., Kvambekk, A., 1998. Monitoring ice thickness in Fram Strait. *J. Geophys. Res.* 103 (C5), 10,437–10,449.
- Wadhams, P., 2000. *Ice in the Ocean*. Gordon and Breach, 351 pp.
- Wadhams, P., Wilkinson, J.P., McPhail, S.D., 2006. A new view of the underside of Arctic sea ice. *Geophys. Res. Lett.* 33 (4) Art. No. L045.
- Weeks, W.F., Ackley, S.F., 1986. The growth, structure, and properties of sea ice. In: Untersteiner, N. (Ed.), *The Geophysics of Sea Ice*. Plenum, pp. 9–164.
- Winebrenner, D.P., Farmer, L.D., Joughin, I.R., 1995. On the response of polarimetric synthetic-aperture radar signatures at 24-cm wavelength to sea-ice thickness in Arctic leads. *Radio Sci.* 30 (2), 373–402.
- Worby, A.P., Griffin, P.W., Lytle, V.I., Massom, R.A., 1999. On the use of electromagnetic induction sounding to determine winter and spring sea ice thickness in the Antarctic. *Cold Reg. Sci. Tech.* 29, 49–58.
- Yu, Y., Maykut, G.A., Rothrock, D.A., 2004. Changes in the thickness distribution of arctic sea ice between 1958–70 and 1993–97. *J. Geophys. Res.* 109, C08004. doi:10.1029/2003JC001982.
- Zwally, H.J., Yi, D., Kwok, R., Zhao, Y., in press. ICESat measurements of sea-ice freeboard and estimates of sea-ice thickness in the weddell sea. *J. Geophys. Res.* doi:10.1029/2007JC004284.